

# Theoretically predicted structures of plasma membrane $\text{Ca}^{2+}$ -ATPase and their susceptibilities to oxidation

Gerald H. Lushington<sup>a,\*</sup>, Asma Zaidi<sup>b</sup>, Mary L. Michaelis<sup>b</sup>

<sup>a</sup> *Molecular Graphics and Modeling Laboratory, University of Kansas, 1251 Wescoe Hall Dr., Lawrence, KS 66045, USA*

<sup>b</sup> *Department of Pharmacology and Toxicology, University of Kansas, 1251 Wescoe Hall Dr., Lawrence, KS 66045, USA*

Received 14 March 2005; received in revised form 22 July 2005; accepted 31 July 2005

Available online 19 September 2005

## Abstract

Oxidative damage to the plasma membrane  $\text{Ca}^{2+}$ -ATPase (PMCA) appears to contribute to the decreased clearance of intracellular  $\text{Ca}^{2+}$  in the neurons of aged brain, possibly contributing to its vulnerability to numerous age-related diseases such as Alzheimer's disease. The precise sites of oxidative susceptibility have not been identified. However, it is known that calmodulin (CaM) protects the purified PMCA against oxidative inactivation, perhaps via conformational restructuring of the protein through dissociation of a 20 residue domain (C20W) in the C-terminal region that function as a CaM-binding site. In order to postulate likely oxidation sites and the mechanism underlying the protection offered by CaM, we have generated a three-dimensional model of PMCA via a combination of homology/comparative modeling, threading, protein–protein docking, and guidance from prior biochemical and analytical studies. The resulting model was validated based on surface polarity/hydrophobicity profiling, standard ProCheck, WhatIF, and PROVE checks, as well as comparison with empirical structure–function observations. This model was then used to identify likely oxidation sites by comparing time-averaged solvent accessibility of potentially oxidizable surface residues as measured from molecular dynamics simulations of intact PMCA and the PMCA sequence from which C20W has been deleted. The resulting model complex has permitted us to identify three amino acids whose solvent accessibility is greatly reduced by the C20W dissociation: Tyr 589, Met 622, and Met 831. © 2005 Elsevier Inc. All rights reserved.

**Keywords:** Plasma membrane  $\text{Ca}^{2+}$ -ATPase; Calmodulin; PMCA; Oxidation; Homology modeling; Threading; Molecular dynamics

## 1. Introduction

Calcium ( $\text{Ca}^{2+}$ ) is a biologically critical trace mineral that functions as a second messenger molecule and regulates a number of important cellular processes as diverse as neurotransmission, hormone secretion, blood clotting, and muscle contraction [1]. Numerous cellular signaling events are contingent upon careful control of the intracellular concentration of free  $\text{Ca}^{2+}$  at specific locations within cells. Such cellular regulation of  $\text{Ca}^{2+}$  is accomplished via different proteins, such as the sarcoplasmic/endoplasmic reticulum  $\text{Ca}^{2+}$ -ATPase (SERCA), the secretory pathway specific  $\text{Ca}^{2+}$ -ATPase (SPCA), the  $\text{Na}^+/\text{Ca}^{2+}$  exchanger, and the plasma membrane  $\text{Ca}^{2+}$ -ATPase (PMCA) [2–4]. Both SERCA and SPCA serve an intracellular buffering role by sequestering excess  $\text{Ca}^{2+}$  from the cytosol into vesicular organelles and releasing it in response to specific signaling events [5,6]. The  $\text{Na}^+/\text{Ca}^{2+}$  exchanger and

PMCA, on the other hand, collaboratively effect the translocation of  $\text{Ca}^{2+}$  across the plasma membrane to the extracellular medium, against a  $10^4$ -fold gradient. The  $\text{Na}^+/\text{Ca}^{2+}$  exchanger is a high capacity but low affinity  $\text{Ca}^{2+}$  transporter and is responsible for bulk ion transport, reducing cytosolic  $\text{Ca}^{2+}$  to about  $1\text{ }\mu\text{M}$ . The PMCA, on the other hand, is a low capacity but high affinity  $\text{Ca}^{2+}$  transporter and accomplishes the finer task of maintaining free cytosolic  $\text{Ca}^{2+}$  at  $\sim 0.1\text{ }\mu\text{M}$ , a concentration considered to be the resting level in most cells [7].

The PMCA and SERCA belong to the family of P type ATPases characterized by the formation of a phosphorylated intermediate [8–10]. Ion transport is thought to be achieved by alterations in the affinity and accessibility of the transmembrane  $\text{Ca}^{2+}$  binding sites [11–13]. The classical E1/E2 hypothesis states that in the E1 state, the binding sites have high affinity for  $\text{Ca}^{2+}$  and open to the cytoplasmic side, whereas in the E2 state, the binding sites have low affinity for  $\text{Ca}^{2+}$  and face the extracellular side in PMCA and the luminal side in SERCA [11–15]. Like the SERCA, PMCA has 10 putative

\* Corresponding author. Tel.: +1 785 864 1140; fax: +1 785 864 5326.

E-mail address: [glushington@ku.edu](mailto:glushington@ku.edu) (G.H. Lushington).

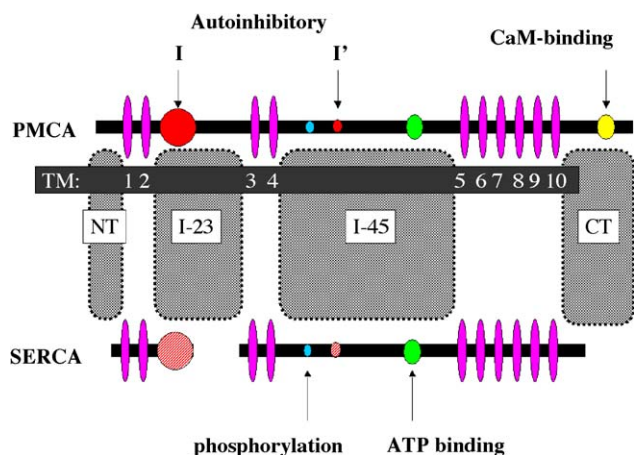


Fig. 1. A schematic showing the functional domains of PMCA and SERCA in terms of aligned sequences. Transmembrane helices are shown in magenta, PMCA auto-inhibitory domains are red (corresponding SERCA sequence analogues are red-striped), the ATP binding and phosphorylation sites are green and cyan, respectively, and the CaM-binding domain is yellow.

transmembrane helices (TM1–TM10) and several functional domains located in the cytosolic portion of the protein, shown in schematic form in Fig. 1. A large intracellular segment between TM4 and TM5 contains the active site of PMCA, comprised of the ATP binding site and an aspartate residue that undergoes phosphorylation during the reaction cycle. The activity of PMCA is regulated by an auto-inhibitory domain located near the C-terminus of the enzyme [16–18]. In the resting state of PMCA, this domain is believed to associate with the catalytic core, thus blocking ATP binding and hydrolysis. The  $\text{Ca}^{2+}$  pumping activity of PMCA is substantially enhanced through interactions with calmodulin (CaM), the ubiquitous  $\text{Ca}^{2+}$  sensor present in all cells [16]. CaM binds to a stretch of 20 amino acid residues (C20W) comprising the CaM-binding domain located near the C-terminus of PMCA [19,20]. The binding of CaM to this region of the PMCA results in the dissociation of the auto-inhibitory domain from the active site, thus relieving the inhibition and allowing for a several-fold increase in activity. PMCA activity can also be stimulated by the  $\text{Ca}^{2+}$ -activated protease calpain that cleaves the CaM-binding domain, leaving a constitutively active 124 kDa fragment of the  $\text{Ca}^{2+}$  pump [21,22]. This mechanism of irreversible stimulation of the calcium pump has been hypothesized to occur in vivo as a defense mechanism against sustained high levels of  $[\text{Ca}^{2+}]$  [21].

Recent evidence implicates a reduction in PMCA–CaM activity as a factor in age-related alterations in  $\text{Ca}^{2+}$  handling observed in brain using several experimental paradigms. Specifically, both PMCA [23,24] and CaM [25] have been found to be highly susceptible to oxidative stress. Exposure of PMCA and CaM to oxidants leads to structural changes in these proteins and results in loss of activity that may be correlated with age-related disturbances in  $\text{Ca}^{2+}$  homeostasis [26]. Instances of sulfoxidized methionine [27,28] and nitrated tyrosine residues [29] on CaM have been reported in aged brain and after in vitro exposure to oxidative stress. However, little is

known about the residues in PMCA that are susceptible to oxidative modification, even though the PMCA appears to be the most sensitive of the known  $\text{Ca}^{2+}$ -transporting proteins to reactive oxygen species [23,30]. Interestingly, the susceptibility of PMCA to the oxidant  $\text{H}_2\text{O}_2$  is mitigated by prior exposure to CaM [23]. Although the precise mechanism underlying protection of PMCA by CaM is unknown, it is reasonable to surmise that PMCA–CaM interaction leads to a conformational restructuring of PMCA that effectively buries susceptible residues. The most obvious effect that CaM-binding is known to exert on the PMCA structure is the dissociation of C20W, the auto-inhibitory CaM-binding domain, corresponding to L1086–D1105 for the human PMCA 4 isoform. This sequence was identified as the major CaM-binding domain via proteolysis studies and subsequent NMR resolution of the resulting C20W–CaM complex [19,20,31]. It is reasonable to expect that a significant structural relaxation will take place upon dissociation of the C20W region from the intracellular loops that constitute the transduction and catalytic domains of the enzyme, and that the resulting structure might shield a number of otherwise oxidatively susceptible residues.

Identification of specific residues that may be protected by CaM is complicated by the absence of reliable tertiary structural characterization of PMCA. Photolabeling studies [20] indicate that the apo form of PMCA places C20W in close spatial proximity to domain I (residues Q200 → G267, located between TM2 and TM3, containing the transduction domain) and domain I' (C537 → T544, located between TM4 and TM5 containing the catalytic core of PMCA) as shown schematically in Fig. 1. Within these segments one finds four oxidatively sensitive residues including one cysteine (537), two methionines (255, 263) and one tyrosine (216) that would be expected to be in reasonably close proximity to a bound CaM and thus could possibly benefit from CaM-mediated protection. Without more definitive knowledge of the folding of PMCA, the solvent accessibility (and thus inherent vulnerability) of these residues is uncertain, and many other possible oxidation sites remain unidentified. In order to elucidate possible oxidation sites, we have undertaken a molecular modeling study involving structural comparative analysis to predict approximate three-dimensional structures and molecular dynamics simulations to elucidate differences in residue oxidative susceptibility in the full-length PMCA structure relative to the PMCA in which the C20W sequence has been excised.

## 2. Computational methods

As a member of the subfamily of  $\text{Ca}^{2+}$ -transporting ATPases, PMCA is homologous to SERCA, with 31.9% sequence identity along overlapped regions, and a 12.8 significance score according to Needleman–Wunsch alignment [32] via a PMUTATION similarity matrix [33]. It is expected to exhibit substantial structural similarity by virtue of sharing 10 common transmembrane helices of comparable lengths (i.e., each helix length is between 22–46 residues for PMCA and 23–41 residues for SERCA), as well as similar-sized interhelical

domains. All extracellular interhelical segments are short loops (8–23 residues) in both PMCA and SERCA, as are all cytosolic helical-bridging strands, except for two substantial lobes (present in both proteins) between the TM2/TM3 and TM4/TM5 transmembrane helices. These lobes will hereafter be referred to as I-23 and I-45, respectively. The secondary structural content of these two cytosolic lobes has also been found to be similar in the two proteins. SERCA, for which crystal structures are available [11–13,34], may thus be considered a reasonable template for comparative modeling of much of the PMCA structure. Exhaustive Swiss-Model searches [35] failed to identify any other viable templates with greater than 25% sequence identity across the global extent of the PMCA sequence.

Three significant portions of the PMCA sequence are not well represented in its alignment with SERCA: a 45 residue section of N-terminal (NT) lobe with an unknown function, a 76 residue portion of the I-23 lobe containing the phospholipid binding site, and the bulk (180 of the last 192 residues) of the C-terminal (CT) domain including the CaM-binding site. Swiss-Model searches on each of these three sequence fragments failed to identify obvious homologous matches for these three lobes.

Since homology is by no means the only indicator of structural similarity among proteins, significant work has been done to devise methods that account for other factors in the evaluation of prospective structural templates, including physicochemical descriptors such as surface electrostatic profile, native energy, solvation energy, and probable secondary structure (e.g., [36]). Such algorithms form the basis for the technique known as ‘Threading’. Given the lack of tangible homologous templates for the NT, I-23, and CT lobes of PMCA, we applied threading analysis, as implemented in the Threader program to determine suitable templates [36]. In each case, a threading search across the entire Threader database was carried out to reveal the top matches as a function of a consensus score covering similarities in native energy, solvation energy, predicted secondary structure (according to PsiPred analysis [37] of the target sequences), sequence similarity, and number of aligned residues. Among the matches identified, those resulting in Z-scores of +2.7 or greater (after adjustment for obvious flaws such as large gaps) with respect to the corresponding PMCA segment were retained. A second threading iteration was then performed in which the target

sequence was threaded only against the subset of initial matches derived from the first iteration. This latter analysis inherently results in lower Z-scores due to the fact that discrimination was being made between members of a much smaller subset, of which all had fairly good initial scores relative to the full database. Thus, we opted to retain templates with adjusted final Z-scores of at least +0.5. The resulting templates are reported in Table 1. For NT, these templates include an archaeal intein-encoded homing endonuclease  $\pi$ -Pfui of *Pyrococcus furiosus* (PDB code: 1DQ3) [38] and an *E. coli* enzyme (1FVK chain A) required for disulfide bond formation in secreted proteins [39]. For I-23, the one template ascertained was a human monocyte chemoattractant protein (1DOK chain A) [40]. For CT, the three templates included the yeast initiation factor 4A N-terminal domain (1QVA) [41], the *E. coli* metal-free isopentenyl diphosphate:dimethylallyl diphosphate isomerase (1HZT) [42], and the pyruvate kinase from rabbit muscle (1A49 chain A) [43]. In addition to the above list of templates, a structural model of the aforementioned C20W–CaM complex (PDB entry 1CFF) as resolved via NMR measurements [31] was used as a template in constructing the CT model. This was done to help ensure that the known primarily helical secondary structure of the CaM-binding site would be preserved in the predicted CT domain model.

Judging from the sequence BLOSUM-62 [44] similarity scores of the templates listed in Table 1, only 1dq3A2 and 1qvaA0 have the relatively large positive scores that indicate probable homology with the NT and CT PMCA domains, respectively. Those templates with BLOSUM-62 scores near zero or with negative values are clearly not homologous with their targets but did show strong correspondences in predicted secondary structures relative to the target lobes. Specifically, among the non-homologous templates, between 65.6 and 91.8% of all residues aligned to the target PMCA domains are predicted to conserve secondary structure with the target. For this reason, their retention as models for guiding the assignment of PMCA secondary structure is reasonable. The 1fvkA1 template for NT also exhibits an excellent 93.3% score for residues aligned with the target sequence, thus signaling minimal sequence gaps and suggesting its value as a model for the overall fold of the NT domain. In multiple sequence alignments derived from the Threader output, the two templates for the NT lobe provide complete coverage of all residues not aligned to the SERCA framework. The three CT templates

Table 1

Threading scores and statistics for the domain templates of the three PMCA cytosolic (N-terminal, I-23, and C-terminal) lobes absent from the SERCA structure

Lobe	Name, CATH code (ref)	Initial Z-score	Final Z-score	BLOSUM 62 score	Number aligned residues	Structure aligned (%)	Sequence aligned (%)
NT	$\pi$ -Pfui endonuclease, <b>1dq3A2</b> [38]	2.78	1.48	22.3	44/45	55.7	97.8
	Disulfide bond formation protein, <b>1fvkA1</b> [39]	2.83	1.10	−6.8	43/45	65.6	93.3
I-23	Monocyte chemoattractant protein, <b>1doka0</b> [40]	2.86	0.71	−35.9	59/76	83.3	78.9
CT	Yeast initiation factor 4A, <b>1qvaA0</b> [41]	3.54	0.85	28.6	147/192	69.0	76.6
	IPP:DMAPP isomerase, <b>1hztZ0</b> [42]	2.92	0.65	3.4	134/192	91.8	69.8
	Pyruvate kinase, <b>1a49A3</b> [43]	3.19	0.50	−18.2	117/192	86.7	60.9

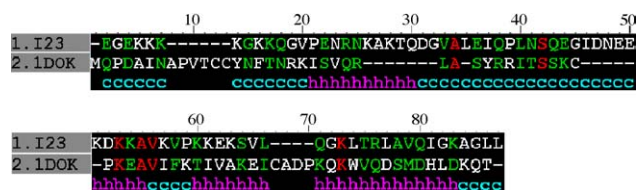


Fig. 2. Alignment between the I-23 lobe of PMCA and the template model 1DOK chain A (human monocyte chemoattractant protein) showing consensus predicted secondary structure for I-23. The amino acid sequences are shown as capital letters colored either as red (identical residue), green (similar) or white (dissimilar). Secondary structure predictions are shown as small letters colored either cyan (coils) or magenta (helices).

collectively cover all residues except for the final eight at the extreme C-terminal end. These last eight residues are predominantly hydrophilic and are assumed to have a disordered structure [45]. Therefore, it is reasonable to assume that they are surficial (or near-surficial) and that their structural resolution is thus amenable to the use of techniques such as simulated annealing. The only PMCA lobe for which tangible gaps exist among template representations, therefore, is I-23. Fortunately, as is shown in Fig. 2, the unrepresented residues are fairly well spread out among four separate gaps in the template/target sequence alignment generated by Threader, with no single gap spanning more than seven residues. Without large or concentrated gaps, it is reasonable to believe that basic folding patterns will be fairly well predicted.

The six templates identified by threading (Table 1) were used in conjunction with SERCA crystal structures to predict the structures of the human PMCA4 isoform in E1 (high affinity for  $\text{Ca}^{2+}$  and ATP) and E2 (low affinity for  $\text{Ca}^{2+}$  and unable to bind ATP) conformational states. The crystal structure corresponding to the E1 and E2 states of SERCA were used as templates [11–13,34]. In both cases, a sufficient portion of the NT and I-23 lobes is present within the SERCA framework (49.6 and 57.5%, respectively) to clearly surmise how those lobes should be spatially arranged within the PMCA structure. However, the absence of 93.8% of the CT domain in the SERCA template framework leads to uncertainty regarding the packing of CT residues with respect to the rest of the PMCA structure. As a result, we chose to generate distinct comparative models of the CT as a separate unit, and of PMCA in the absence of CT (hereafter referred to as PMCA CT (–)) and then to fit CT into the PMCA CT (–) framework via simulated protein–protein docking.

As a preparation for comparative modeling, target–template alignments were effected via the Clustal-W program [46], using the BLOSUM-30 substitution matrix [44], and standard gap penalties of 10 for opening and 0.1 for extension. Alignment between PMCA and the SERCA framework was carried out in a piecemeal fashion, with each distinct transmembrane helix and interhelical loop or lobe being aligned separately in order to ensure preservation of bulk features. This strategy was based on the partitioning and characterization of PMCA by Penniston and Enyedi [45], and by Carafoli [7]. Comparative models for CT and for the E1 and E2 versions of PMCA CT (–), one based on the E1 SERCA template and the second on the E2 SERCA,

were then constructed via the Modeller program [47]. Default restraint settings were retained, and rigorous simulated annealing steps using the CHARMM force field and charges [48] were employed to permit reasonable co-integration of the structural features dictated by the different templates. Specifically, five simulated annealing cycles of 4.4 ps stepwise warming ( $0 \rightarrow 150 \rightarrow 250 \rightarrow 400 \rightarrow 700 \rightarrow 1000$  K) followed by 19.2 ps stepwise cooling ( $1000 \rightarrow 800 \rightarrow 600 \rightarrow 500 \rightarrow 400 \rightarrow 300$  K) were performed. In order to achieve a rough estimate of the accessible conformational space, 10 distinct structures were generated for each of the two PMCA CT (–) conformers, via 10 distinct simulated annealing runs, each starting with a different random seed.

In order to merge the CT domain with each of the PMCA CT (–) conformers, a structure composed of the final 172 residues of the 192 residue comparative model for CT was docked into each of the 10 PMCA CT (–) conformers for each of the E1 and E2 forms of PMCA. The first 20 residues of CT were omitted from initial consideration so that they could be used later to reconnect the chain (via simulated annealing) in a minimally strained fashion. The docking was performed via the GRAMM program [49] with standard low-resolution settings of  $\eta = 6.8$ ,  $r_0 = 6.5$  Å.

For each docking simulation, 1000 distinct possible complexes were generated and ranked according to approximate interaction energy. Neither the E1 nor E2 states produced results pointing to a single complex with obviously superior energy, but instead yielded a diverse spread of different prospective structures. In order to evaluate these structures, the top 10 scoring complexes were isolated from the GRAMM output of each run, and were statistically analyzed in energetically weighted distributions of the translation and rotation coordinates of the docked CT structures relative to their initial coordinates. These distributions are reported in Figs. 3 and 4.

The translational and rotational coordinate distributions reported in Figs. 3 and 4 reflect the presence of several families of docked structures. The most prevalent families, i.e., those with the highest vertical bars for the translational and rotational coordinates, for both the E1 and E2 states correspond to structures shown in Figs. 5A and 6A that are not biophysically realistic: the CT structure binds on the exterior of the PMCA CT (–) structure, with a substantial portion impinging on the transmembrane region of the latter. The main reason such non-physical structures arise from the modeling appears to be an affinity between significant hydrophobic patches on the CT surface and the inherently lipophilic surface of the transmembrane region. In a real intracellular environment, such an interaction would be impossible due to the presence of other membrane proteins or lipids in close physical association with the PMCA TM domain, collectively forming the contiguous membrane shown schematically in Figs. 5 and 6 with magenta stripes. Such molecules are not explicitly represented in our model due to unavailability of relevant membrane templates. Thus, the models judged to impinge excessively on the membrane location were discarded. Among the remaining structures, one family indicated with gray boxes on Figs. 3 and



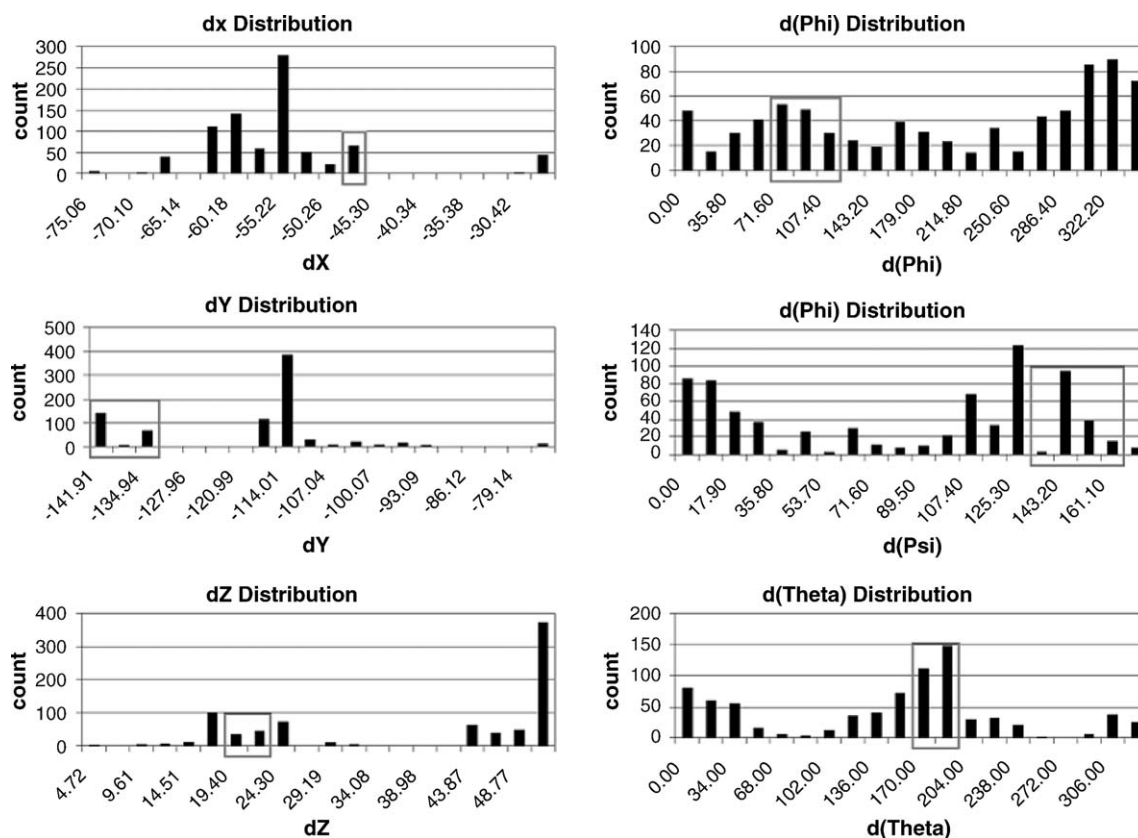


Fig. 3. Energy-weighted prevalence of translational and rotational displacements (relative to the Cartesian coordinate origin) for the docking of CT to the E1 PMCA CT (–) framework. The family of structures agreeing best with experimental observations is indicated by gray boxes.

4, is particularly compelling because it places the C20W fragment of CT in close proximity to both the I and I' domains of the PMCA CT (–) framework (Figs. 5B and 6B), consistent with prior experimental predictions [20,50]. This latter structural family best satisfies current empirical knowledge of the inter-domain interactions of both the E1 and E2 states of PMCA. Consequently, we have used representative models from this family, chosen to be as close as possible to the median of the family's coordinate distributions, as the basis of our ensuing models of E1 and E2 PMCA.

Docked CT/PMCA CT (–) complexes were merged to form unified PMCA models via the Modeller program [47]. The complex was used as the structural template, and the corresponding sequence alignment was a direct projection of these units on the complete PMCA sequence. The collective structure of 20 residues in the gap between the two fragments was solved via steric and bond energy considerations conveyed by the CHARMM force field [48]. The same simulated annealing protocol used to assemble models for the initial CT and PMCA CT (–) units was then applied in order to smoothly integrate the distinct units and to relax the 20 residue-bridging strand.

CaM interaction with PMCA is known to induce a decoupling (termed 'dissociation') of the CaM-binding site from the main PMCA-fold [19]. Three-dimensional structures of such a complex are not available. However, because this C20W dissociation is known to lead to stimulation of the

ATPase activity of the protein [50] that is qualitatively similar to that observed when this portion of the protein has been fully proteolyzed via calpain [20], it is reasonable to assume that the PMCA/CaM complex entails substantial separation of the C20W strand from the primary PMCA structure. Given this useful knowledge, we have prepared a model for the modified form of E1 PMCA wherein C20W has been dissociated (hereafter to be referred to as PMCA C20W (–)) by removing the C20W residues from the predicted PMCA E1 structure and terminating the truncated residues Glu1085 and Val1106 as a neutral acid and base, respectively. Both the PMCA and PMCA C20W (–) structures were then protonated via the X-LeaP program distributed within the AMBER 8 software suite [51,52]. For all calculations, glutamate and aspartate monomers were modeled in their anionic forms, lysines and arginines were described as cations, N<sup>δ</sup>s on histidines were protonated, while N<sup>ε</sup>s were left in the unprotonated sp<sup>2</sup> hybridized form. All other residues were left in their neutral forms. Negative charges were balanced with Na<sup>+</sup> ions added according to a coulomb potential on a 1.0 Å grid. Both structures were then optimized for 1000 steps in AMBER 8 via the parm99 force field [53]. The resulting refined structures were then dynamically warmed in AMBER 8 from 100 to 300 K over the course of a 100 ps generalized Born dynamics simulation [54]. These equilibrated structures were then subjected to a 1.0 ns generalized Born dynamic simulation at 300 K in order to achieve reasonable time-averaged sampling. Trajectory snapshots were extracted

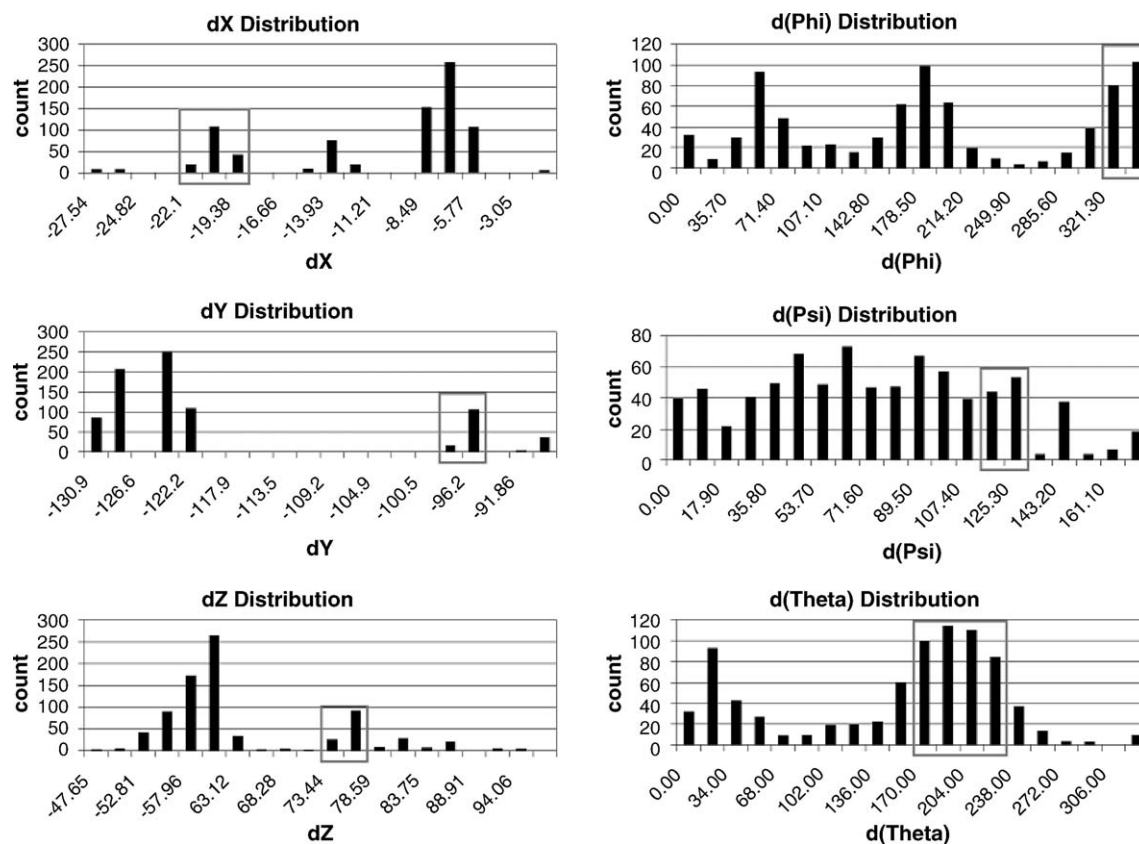


Fig. 4. Energy-weighted prevalence of translational and rotational displacements (relative to the Cartesian coordinate origin) for the docking of CT to the E2 PMCA CT (–) framework. The family of structures agreeing best with experimental observations is indicated by gray boxes.

from every 2.0 ps for analysis of residue solvent accessible surface area with the DMS program (a utility of the Midas Plus suite [55]). Mean values for the solvent accessible surface area of each residue were determined as simple averages over all 500 snapshots, and the error margin was set equal to  $\pm 1$  standard deviation.

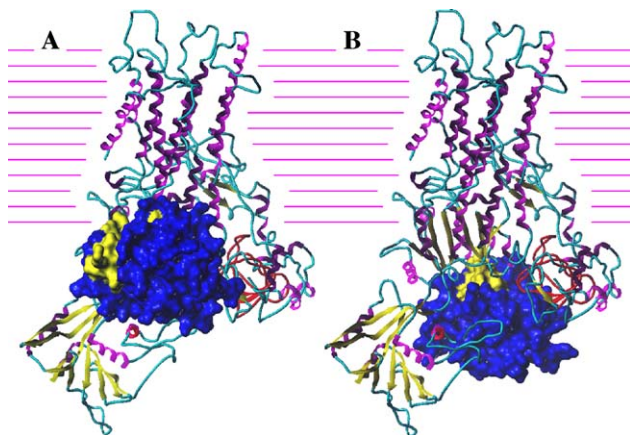


Fig. 5. Characteristic structures for the most prevalent (A) and most experimentally plausible (B) families of CT docked to E1 PMCA CT (–). PMCA CT (–) is rendered so that yellow arrows represent  $\beta$ -sheets, magenta ribbons indicate  $\alpha$ -helices, and cyan tubes convey unstructured coils. Both I and I' domains are shown in red. CT is shown as a blue solid, with the C20W fragment rendered in yellow. Magenta horizontal bars convey an estimated extent of the membrane, as depicted by the location of the 10 PMCA TM helices.

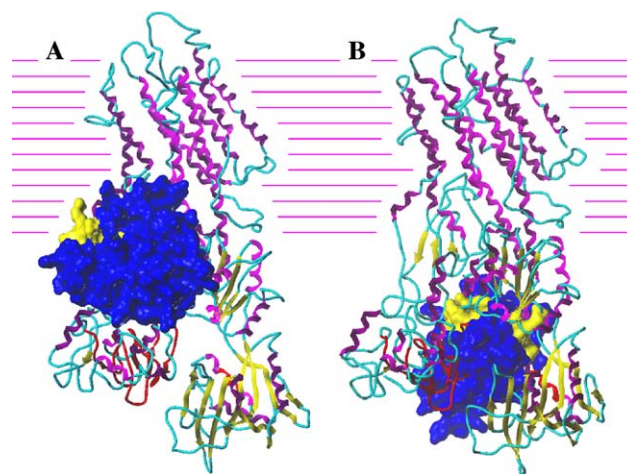


Fig. 6. Characteristic structures for the most prevalent (A) and most experimentally plausible (B) families of CT docked to E2 PMCA CT (–). E2 PMCA CT (–) is rendered so that yellow arrows represent  $\beta$ -sheets, magenta ribbons indicate  $\alpha$ -helices, and cyan tubes convey unstructured coils. Both I and I' domains are shown in red. CT is shown as a blue solid, with the C20W fragment rendered in yellow. Magenta horizontal bars convey an estimated extent of the membrane, as illustrated by the location of the 10 PMCA TM helices.

### 3. Results and discussion

The structures predicted for E1 and E2 PMCA were subjected to detailed analysis by the PROCHECK [56], PROVE [57], and WhatIF [58] structure validation suites. Both

structures score reasonably well on most structural criteria, and thus give us reasonable confidence in the general plausibility of the models. Among the criticisms raised by these utilities is that atomic volume validation analysis from PROVE flags numerous individual atoms as having unrealistically large associated volumes, and scores both molecules as “bad” in this respect. The main explanation for this is that our predicted structures possess numerous small voids (1.0–5.0 Å in diameter) at the boundaries of the four sizeable cytosolic lobes. These lobes biologically interact with each other in a dynamic, mobile fashion and conformationally restructure in the process of normal protein function, and thus they are unlikely to be optimally packed. Also, the fact that we have not attempted to account for *in situ* water molecules in the structure seems to have led to a significant number of unsatisfied H-bond donor and acceptor sites according to WhatIF analysis. Finally, WhatIF evaluation of van der Waals contacts indicates the presence of numerous steric clashes at the boundary of the docked CT domain. A significant number of strained PROCHECK bond and angle values are also present in this region. Since unchaperoned protein folding frequently occurs within a time frame of minutes–hours, the question of the length of molecular dynamics simulation required to fully alleviate such domain-packing stresses is open-ended. Thus, there are some approximations in our model that limit the scope of our predictions to general attributes such as elucidation of inter-domain associations, formation of approximate, low-resolution protein–protein complexes, and identification of probable surface accessible residues.

The Connolly solvent accessible surface (1.4 Å probe) for our predicted structure of the E1 PMCA conformer, showing surface electrostatic and hydrophobic features, is depicted in Fig. 7. Visual inspection of the chemical functionality of surface residues reveals that the transmembrane surface is predominantly lipophilic, whereas the cytosolic and extracellular surfaces are mostly polar. This is an important point of

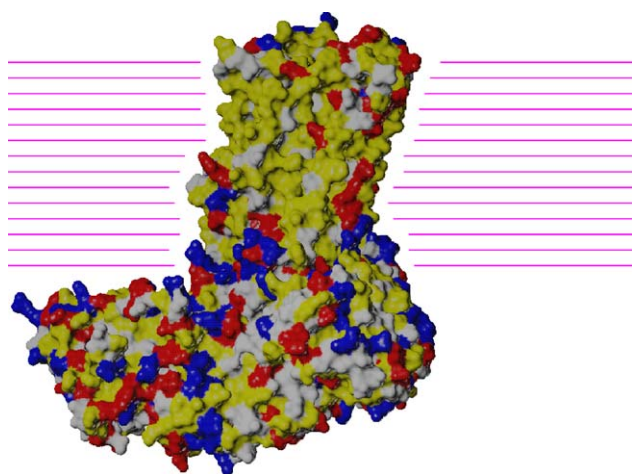


Fig. 7. Connolly surface representation of PMCA colored by residue chemical functionality. Yellow surfaces are hydrophobic, red are acidic, blue are basic, and white are polar-neutral. Magenta horizontal bars convey an estimated extent of the membrane, as illustrated by the location of the 10 PMCA TM helices.

Table 2

Hydrophobic surface area as a percentage of total surface area for the PMCA transmembrane region, solvated regions, and total protein

PMCA conformer	TM	Solvated (cytosolic + extracellular)	Entire PMCA
E1 (%)	66.1	38.8	44.4
E2 (%)	64.4	38.6	44.2

validation, helping to confirm that the various domains of the predicted structure obey a reasonable solvation profile. This offers reassurance that the original sequence/structure alignment, the choice of templates, and the general domain-packing collectively yield a physicochemically reasonable structure. Table 2 provides quantitative confirmation of this assertion by demonstrating that the percent hydrophobic surface as a function of enzyme region for both the E1 and E2 conformers reflects a net lipophilic transmembrane region and aqueous soluble cytosolic lobes. Specifically, hydrophobic residues constitute nearly two-thirds of the contact surface area of the transmembrane domains in both the E1 and E2 PMCA structures, while comprising less than 40% of the surfaces of cytosolic and extracellular regions.

Important enzymatic features of our predicted structures for E1 and E2 PMCA are shown in Fig. 8. In comparing the two forms, one observes that the cytosolic domains ( $\beta$ -sheet-rich lobes near the bottom) exhibit substantially different spatial packing as a function of bulk conformation. As is the case with SERCA [11–13,34], the cytosolic lobes in the E1 form of PMCA tend to be flattened upwards onto the membrane region, whereas, in the E2 form these same lobes tend to dangle further down into the cytosol. Substantial occlusion of the ATP binding site (in green) and the phosphorylation site (cyan) observed in the E2 conformer may contribute to low affinity for ATP and is consistent with previous observations that release of cations into the extracellular or luminal side occurs while the enzyme is still phosphorylated [9]. In contrast, the E1 structure appears to afford substantially greater solvent and substrate accessi-

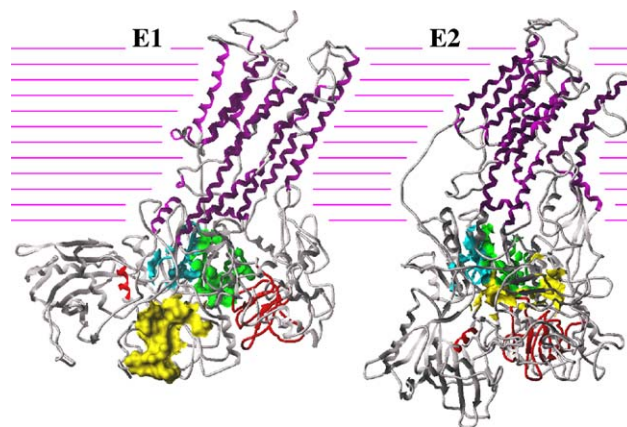


Fig. 8. Functional domains of E1 and E2 PMCA conformers. Transmembrane helices are colored magenta, while the solvent accessible surfaces of C20W, I + I' domains, and the ATP binding and phosphorylation sites are yellow, red, green, and cyan, respectively.



bility to the known ATP binding and phosphorylation sites, consistent with the observed enzymatic activity [50]. The CaM-binding site (C20W, shown in yellow) is also significantly more exposed in the E1 form. Interestingly, the CaM-binding residues adopt a substantially different orientation with respect to the auto-inhibitory domains in the E1 and E2 structures: in the E1 form, the C20W helix is proximate to, but not in direct contact with either **I** or **I'** (red) whereas, for the E2 conformer, the CaM-binding site has been rotated so that its two ends simultaneously couple directly with both **I** and **I'**. Among the members of the family of structures derived from CT/E1 PMCA CT (–) docking simulations, no candidate PMCA structures exhibit this direct C20W overlap with **I** and **I'**. However, direct overlap between C20W with one or both of these domains tends to be a consistent feature of the family of structures resulting from CT docking into the E2 PMCA CT (–) structure. The structural difference in the orientation of the auto-inhibitory domain between E1 and E2 states may account for the basal PMCA activity observed in the absence of CaM. It can be speculated that binding of CaM to PMCA may further dissociate C20W away from the active site thus increasing the accessibility of the ATP binding site and yielding several-fold stimulation of PMCA activity. This feature appears to agree very well with single molecule polarization studies that established a correlation between strong **I** + **I'**/C20W overlap in the E2 PMCA structure and its poor affinity for ATP relative to E1 PMCA [50,59].

The predicted structures of E1 and E2 PMCA conformer extremely well to the functional expectation of the first state as having a high affinity for  $\text{Ca}^{2+}$  binding and the second as being able to release  $\text{Ca}^{2+}$  from the extracellular surface of the protein. Specifically, one sees in Fig. 9 that the E1 conformer, when viewed from below the cytosolic domains, contains a linear channel that projects all the way from the cytosol through

the transmembrane domain and out to the extracellular environment. Without extensive molecular dynamics analysis it is not possible to make definitive statements regarding the precise ion transport mechanism; however, there are some aspects of the channel that deserve mention. First, there are three phenylalanine side chains (800, 1116, 1146; not shown) in the lower half of the channel, with the latter two appearing near the bottom of the cytosolic region and Phe 800 existing near the base of the transmembrane domain. Given the propensity of the Phe for ring-flipping, it is possible that these side chains perform some type of valve function to help regulate ionic flow. Most of the rest of the residues whose side chains occupy space within the channel are either polar or small non-polar species that should do little to impede ion transport. The ion-sequestering site (lower diagrams in Fig. 9) is in approximately the same location in our predicted structures for PMCA as was observed for SERCA: along the channel about half way up the transmembrane domain [11–13,34]. However, unlike SERCA in which the  $\text{Ca}^{2+}$  binding site is tetra-anionic and spatially suitable for two  $\text{Ca}^{2+}$  ions, the PMCA site is only dianionic (Glu 423 + Asp 883). However, it does also have two nearby carbonyls present (on the Val 419 backbone and Gln 851 side chain) that may be capable of helping to stabilize a dication. This agrees with assertions that PMCA pumps only one  $\text{Ca}^{2+}$  ion at a time, as opposed to two for SERCA [45]. Based on Fig. 9, E2 possesses no linear channel comparable to that of E1. The substantial rearrangement of both cytosolic and transmembrane folds significantly disrupts the linearity of the channel-forming segments, and occludes the cytosolic entrance. The ion sequestering site in E2 is also substantially disrupted, with our predicted structure showing the anionic Glu 423 and Asp 883 side chains to have become separated ( $\sim 13.4$  Å between carboxy groups) rendering the site unsuitable for  $\text{Ca}^{2+}$  retention. Whereas the two helices TM3 and TM7 appear to serve as part of the channel wall around the E1 sequestering site, one finds in E2 that the two helices are spread substantially apart, leaving the site exposed, possibly creating a portal for  $\text{Ca}^{2+}$  release on the opposite side. Similar observations have been made with respect to the SERCA structure [11–13,34], wherein significant separation between TM3 and TM7 is also observed. The average distance between the four ion sequestering carboxyl carbons increases from 7.06 Å for E1 to 10.25 Å for E2.

From the static PMCA E1 structure, generalized Born dynamics simulations were used to explore the flexibility of the protein surface and obtain an estimate of the possible oxidative susceptibility of each cysteine, methionine, and tyrosine residue located within the PMCA cytosolic domains (NT, I-23, I-45, and CT). The susceptibility was ascertained as a function of the percent of time during which part of the residue was solvent exposed and the average solvent accessible surface area of the residue during this time. Error bars for the latter were derived as simple standard deviations. In total, 40 different cysteine, methionine, and tyrosine residues were identified as being partially accessible for a portion of the dynamics simulations of PMCA and PMCA C20W (–). This list of 40 was condensed to a subset of 12 key residues based on

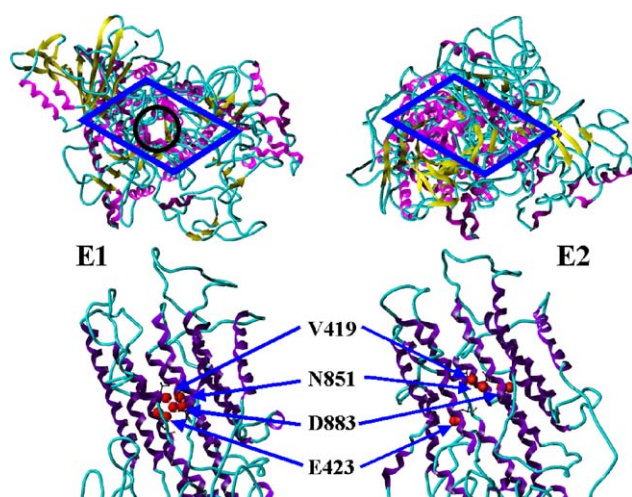


Fig. 9.  $\text{Ca}^{2+}$  channel and binding site for the E1 and E2 PMCA conformers. The upper diagrams view the structure from above the cytosolic portion of PMCA, with the transmembrane domain (highlighted with a blue rhombus) projecting down into the plane of the page. The putative  $\text{Ca}^{2+}$  channel in E1 is circled in black. The lower diagrams are side views of the transmembrane domains showing  $\text{Ca}^{2+}$  binding oxygens as red spheres.



Table 3

Predicted persistence and extent of residue solvent accessibility for key cytosolic cysteine, methionine, and tyrosine residues for PMCA and PMCA C20W (–)

PMCA			PMCA C20W (–)		Differences	
	% of time exposed	Mean area exposed (Å <sup>2</sup> )	% of time exposed	Mean area exposed (Å <sup>2</sup> )	Δ% of time exposed	Δ of mean area exposed (Å <sup>2</sup> )
Met14	100	88.9 ± 9.9	100	43.9 ± 16.8	0.0	–45.0 ± 26.7
Cys24	100	38.8 ± 10.6	100	67.4 ± 5.4	0.0	+28.6 ± 16.0
Tyr48	100	85.8 ± 12.9	100	113.0 ± 12.9	0.0	+27.2 ± 25.8
Met441	0.6	20.3 ± 5.8	41.4	50.0 ± 14.3	+40.8	+29.7 ± 19.1
Met472	100	22.8 ± 9.5	100	56.5 ± 15.9	0.0	+33.7 ± 25.4
Tyr550	100	84.6 ± 16.2	100	124.9 ± 13.5	0.0	+40.3 ± 29.7
<b>Tyr566</b>	0.4	11.2 ± 1.0	100	76.0 ± 13.6	<b>+99.6</b>	<b>+64.8 ± 14.6</b>
<b>Tyr589</b>	100	49.8 ± 17.7	1.8	23.5 ± 10.8	<b>–98.2</b>	Insignificant
<b>Met622</b>	100	46.8 ± 14.7	0.4	47.6 ± 10.5	<b>–99.6</b>	Insignificant
Cys632	100	85.3 ± 8.5	100	71.7 ± 3.3	0.0	–13.6 ± 11.8
Met694	0.6	9.6 ± 3.1	37.5	38.9 ± 17.9	+36.9	+29.3 ± 21.0
<b>Met831</b>	100	48.7 ± 11.2	1.6	15.5 ± 3.8	<b>–98.4</b>	<b>–33.2 ± 15.0</b>

Significant differences between PMCA and PMCA C20W (–) are also reported, with residues exhibiting the most striking changes shown in bold.

adherence to at least one of the following two criteria: (a) a difference in the mean solvent accessibility for E1 versus E1 PMCA C20W (–) that was greater than the sum of the standard deviations associated with these means and (b) a difference in persistence of solvent accessibility (i.e., number of snapshots wherein the solvent exposure is non-zero) over the two simulations equal to at least half the total length of the simulation (i.e., at least 250 snapshots). These criteria were chosen to establish substantial statistical and qualitative differences in residue solvent accessibility in the PMCA C20W (–) model versus that found for the normal PMCA. Among these 12 key residues listed in Table 3, fairly clear stratification was evident in the extent to which solvent accessibility differed between the intact PMCA versus the truncated form. Four residues exhibited dramatic qualitative differences that would unquestionably suggest variations in oxidative susceptibility, and the other eight displayed more modest variations of statistical significance, but of uncertain biological impact.

Of those four residues exhibiting large changes, three appear to have dramatically reduced solvent exposure in PMCA C20W (–): Met 831, Met 622, and Tyr 589 that are exposed 100% of the time in the full PMCA simulation (i.e., have non-zero solvent accessible surface area for all 500 snapshots analyzed) become exposed less than 2% of the time in PMCA C20W (–). The other residue, Tyr 566 exhibits the opposite trend, i.e., it is exposed 0.4% of the time in the case of intact PMCA, but becomes exposed 100% of the time in PMCA C20W (–). Solvent accessibility of these four residues in the intact and truncated versions of PMCA is shown graphically as a snapshot at  $t = 1.0$  ns in both cases (Fig. 10). In this instance, Met 831, Met 622, and Tyr 589 are solvent exposed in PMCA while Tyr 566 is not. Conversely, for PMCA C20W (–), Met 831, and Met 622 are completely buried and Tyr 589 has only a small amount of exposed surface area; however, Tyr 566 side chain is nearly completely exposed. Based on this cumulative information and the fact that most reactive oxygen species travel in solvent phase, it appears quite likely that Met 831, Met 622, and Tyr 589 should have reduced oxidative susceptibility after C20W

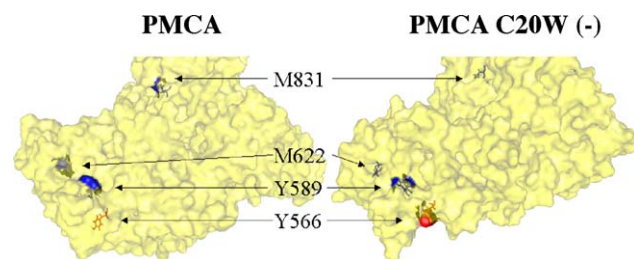


Fig. 10. Solvent accessible surfaces for the cytosolic domains of PMCA and PMCA C20W (–), highlighting the exposed surfaces of three oxidatively susceptible residues (Tyr 589, Met 622, and Met 831; all shown with blue solid surfaces) whose accessibility is diminished in PMCA C20W (–) and one (Tyr 566; shown as red solid) whose accessibility increases upon dissociation of C20W.

has dissociated from the PMCA-fold, whereas Tyr 566 may be somewhat more susceptible.

The eight residues displaying less striking deviation in the PMCA and PMCA C20W (–) simulations, while not supportive of strong arguments regarding relative oxidative susceptibility, deserve some discussion for the sake of possible future experimental testing. Six of these residues (Met 14, Cys 24, Tyr 48, Met 472, Tyr 550, and Cys 632) are predicted to be at least partially exposed during the entirety of both the full PMCA and PMCA C20W (–) simulations, with small but statistically significant differences in average accessible surface areas. Met 441 and Met 694 were completely buried during minor portions of one or both simulations, but have deviations in average accessibility profile that barely exceed the standard error margin. Tentatively, we would suggest that Met 14 and Cys 632 may be less susceptible in the PMCA C20W (–) model, while Cys 24, Tyr 48, Met 441, Met 472, Tyr 550, and Met 694 may be more susceptible to oxidation.

#### 4. Conclusions

PMCA is not a natural choice for computational protein structure modeling because of the absence of known strongly homologous templates for important cytosolic domains such as

the C-terminus. The importance of PMCA to numerous fields of biomedical research is a strong inducement. Relying heavily on prior experimental data regarding inter-domain associations as well as the interaction of PMCA with CaM, we employed a combination of homology modeling, threading, and protein–protein docking techniques to generate an approximate three-dimensional structure that appears to satisfy most experimental observations. Comparison between the predicted structures for E1 and E2 states of PMCA shows significant differences in the accessibility of the  $\text{Ca}^{2+}$  binding sites, ATP binding and phosphorylation sites. We would further suggest that the direct coupling between C20W and the I and I' domains observed in E2 PMCA but not in the E1 form may be a key structural factor in altering the accessibility of the  $\text{Ca}^{2+}$  and ATP binding sites. Such changes in the orientation of the auto-inhibitory domain may account for basal PMCA activity observed in the absence of CaM. Finally, our predicted PMCA (E1) structural model provided us with the basis for 1.0 ns molecular dynamics simulations of the full PMCA as well as the PMCA C20W (–). Detailed survey of the solvent accessibilities of all cytosolic cysteine, methionine, and tyrosine residues over the course of the simulations allowed us to ascertain major changes in accessibility of four residues, including Tyr 566 which is likely to become more susceptible to oxidation, and Tyr 589, Met 622, and Met 831, that appear to receive significant protection from the structural relaxation after C20W dissociation. These latter three may prove to be important in explaining the protective effect that CaM exerts on PMCA against oxidant-induced inactivation; thus, we would recommend them as a focus for further experimental analysis. Although the extent of similar relaxation effects is not large enough in other residues to support firm pronouncements on prospective oxidative susceptibility from our modeling data alone, several others do exhibit statistically significant variations in the simulated solvent accessibility. These include Met 14 and Cys 632, the solvent accessibility profiles of which are also diminished in the PMCA C20W (–) model and thus may also be worthy targets for further study.

## Acknowledgements

This work has been supported in part by NIH Grants AG 12,993 and COBRE RR017708. The authors would like to thank Carey Johnson, Kenneth Osborn, and Brian Slaughter for valuable discussions.

## References

- [1] E. Carafoli, The ambivalent nature of the calcium signal, *J. Endocrinol. Invest.* 27 (2004) 134–136.
- [2] A. Majewska, E. Brown, J. Ross, R. Yuste, Mechanisms of calcium decay kinetics in hippocampal spines: role of spine calcium pumps and calcium diffusion through the spine neck in biochemical compartmentalization, *J. Neurosci.* 20 (2000) 1722–1734.
- [3] E. Carafoli, Calcium signaling: a historical account, *Biol. Res.* 37 (2004) 497–505.
- [4] D. Pietrobon, F. Di Virgilio, T. Pozzan, Structural and functional aspects of calcium homeostasis in eukaryotic cells, *Eur. J. Biochem.* 193 (1990) 599–622.
- [5] D.A. Dixon, D.H. Haynes, Kinetic characterization of the  $\text{Ca}^{2+}$ -pumping ATPase of cardiac sarcolemma in four states of activation, *J. Biol. Chem.* 264 (1989) 13612–13622.
- [6] K. van Baelen, L. Dode, J. Vanoevelen, G. Callewaert, H. de Smedt, L. Missiaen, J.B. Parys, L. Raeymaekers, F. Wuytack, The  $\text{Ca}^{2+}/\text{Mn}^{2+}$  pumps in the Golgi apparatus, *Biochim. Biophys. Acta* 1742 (2004) 103–112.
- [7] E. Carafoli, The plasma membrane calcium pump: structure, function, regulation, *Biochim. Biophys. Acta* 1101 (1992) 266–267.
- [8] K.B. Axelsen, M.G. Palmgren, Evolution of substrate specificities in the P-type ATPase superfamily, *J. Mol. Evol.* 46 (1998) 84–101.
- [9] W. Kuhlbrandt, Biology, structure and mechanism of P-type ATPases, *Nat. Rev. Mol. Cell. Biol.* 5 (2004) 282–295.
- [10] J.V. Moller, B. Juul, M. le Maire, Structural organization, ion transport, and energy transduction of P-type ATPases, *Biochim. Biophys. Acta* 1286 (1996) 1–51.
- [11] C. Toyoshima, H. Nomura, Structural changes in the calcium pump accompanying the dissociation of calcium, *Nature* 418 (2002) 605–611.
- [12] C. Toyoshima, H. Nomura, T. Tsuda, Lumenal gating mechanism revealed in calcium pump crystal structures with phosphate analogues, *Nature* 432 (2004) 361–368.
- [13] C. Toyoshima, T. Mizutani, Crystal structure of the calcium pump with a bound ATP analogue, *Nature* 430 (2004) 529–535.
- [14] L. de Meis, A.L. Vianna, Energy interconversion by the  $\text{Ca}^{2+}$ -dependent ATPase of the sarcoplasmic reticulum, *Annu. Rev. Biochem.* 48 (1979) 275–292.
- [15] R.L. Post, C. Hegyvary, S. Kume, Activation by adenosine triphosphate in the phosphorylation kinetics of sodium and potassium ion transport adenosine triphosphatase, *J. Biol. Chem.* 247 (1972) 6530–6540.
- [16] E. Carafoli, F. Kessler, R. Falchetto, R. Heim, M. Quadroni, J. Krebs, E.E. Strehler, T. Vorherr, The molecular basis of the modulation of the plasma membrane calcium pump by calmodulin, *Ann. N.Y. Acad. Sci.* 671 (1992) 58–68 (discussion 68–59).
- [17] A.J. Caride, N.L. Elwess, A.K. Verma, A.G. Filoteo, A. Enyedi, Z. Bajzer, J.T. Penniston, The rate of activation by calmodulin of isoform 4 of the plasma membrane  $\text{Ca}^{2+}$  pump is slow and is changed by alternative splicing, *J. Biol. Chem.* 274 (1999) 35227–35232.
- [18] N.L. Elwess, A.G. Filoteo, A. Enyedi, J.T. Penniston, Plasma membrane  $\text{Ca}^{2+}$  pump isoforms 2a and 2b are unusually responsive to calmodulin and  $\text{Ca}^{2+}$ , *J. Biol. Chem.* 272 (1997) 17981–17986.
- [19] R. Falchetto, T. Vorherr, J. Brunner, E. Carafoli, The plasma membrane  $\text{Ca}^{2+}$  pump contains a site that interacts with its calmodulin-binding domain, *J. Biol. Chem.* 266 (1991) 2930–2936.
- [20] R. Falchetto, T. Vorherr, E. Carafoli, The calmodulin-binding site of the plasma membrane  $\text{Ca}^{2+}$  pump interacts with the transduction domain of the enzyme, *Protein Sci.* 1 (1992) 1613–1621.
- [21] K.K. Wang, A. Villalobo, B.D. Roufogalis, The plasma membrane calcium pump: a multiregulated transporter, *Trends Cell Biol.* 2 (1992) 46–52.
- [22] K.K. Wang, B.D. Roufogalis, A. Villalobo, Calpain I activates  $\text{Ca}^{2+}$  transport by the reconstituted erythrocyte  $\text{Ca}^{2+}$  pump, *J. Membr. Biol.* 112 (1989) 233–245.
- [23] A. Zaidi, L. Barron, V.S. Sharov, C. Schoneich, E.K. Michaelis, M.L. Michaelis, Oxidative inactivation of purified plasma membrane  $\text{Ca}^{2+}$ -ATPase by hydrogen peroxide and protection by calmodulin, *Biochemistry* 42 (2003) 12001–12010.
- [24] A. Zaidi, M.L. Michaelis, Effects of reactive oxygen species on brain synaptic plasma membrane  $\text{Ca}^{2+}$ -ATPase, *Free Radic. Biol. Med.* 27 (1999) 810–821.
- [25] M.L. Michaelis, D.J. Bigelow, C. Schoneich, T.D. Williams, L. Ramonda, D. Yin, A.F. Huhmer, Y. Yao, J. Gao, T.C. Squier, Decreased plasma membrane calcium transport activity in aging brain, *Life Sci.* 59 (1996) 405–412.
- [26] T.C. Squier, D.J. Bigelow, Protein oxidation and age-dependent alterations in calcium homeostasis, *Front. Biosci.* 5 (2000) D504–D526.
- [27] J. Gao, Y. Yao, T.C. Squier, Oxidatively modified calmodulin binds to the plasma membrane  $\text{Ca}^{2+}$ -ATPase in a nonproductive and conformationally disordered complex, *Biophys. J.* 80 (2001) 1791–1801.

- [28] T. Toda, T. Morimasa, S. Kobayashi, K. Nomura, T. Hatozaki, M. Hirota, A proteomic approach to determination of the significance of protein oxidation in the ageing of mouse hippocampus, *Appl. Genom. Proteom.* 2 (2003) 43–50.
- [29] H.S. Smallwood, N.A. Galeva, R.K. Bartlett, R.J. Urbauer, T.D. Williams, J.L. Urbauer, T.C. Squier, Selective nitration of Tyr99 in calmodulin as a marker of cellular conditions of oxidative stress, *Chem. Res. Toxicol.* 16 (2003) 95–102.
- [30] M. Kaneko, R.E. Beamish, N.S. Dhalla, Depression of heart sarcolemmal  $\text{Ca}^{2+}$ -pump activity by oxygen free radicals, *Am. J. Physiol.* 256 (1989) H368–H374.
- [31] B. Elshorst, M. Hennig, H. Forsterling, A. Diener, M. Maurer, P. Schulte, H. Schwalbe, C. Griesinger, J. Krebs, H. Schmid, T. Vorherr, E. Carafoli, NMR solution structure of a complex of calmodulin with a binding peptide of the  $\text{Ca}^{2+}$  pump, *Biochemistry* 38 (1999) 12320–12332.
- [32] S.B. Needleman, C.D. Wunsch, A general method applicable to the search for similarities in the amino acid sequence of two proteins, *J. Mol. Biol.* 48 (1970) 443–453.
- [33] M. Dayhoff, R.M. Schwartz, B.C. Orcutt, A model of evolutionary change in proteins: matrices for detecting distant relationships, *Atlas of Protein Sequence and Structure*, 5, 1978, pp. 345–358.
- [34] C. Toyoshima, M. Nakasako, H. Nomura, H. Ogawa, Crystal structure of the calcium pump of sarcoplasmic reticulum at 2.6 Å resolution, *Nature* 405 (2000) 647–655.
- [35] T. Schwede, J. Kopp, N. Guex, M.C. Peitsch, SWISS-MODEL: an automated protein homology-modeling server, *Nucleic Acids Res.* 31 (2003) 3381–3385.
- [36] D.T. Jones, Protein sequence threading by double dynamic programming, in: *Computational Methods in Molecular Biology*, Elsevier Science, New York, 1998.
- [37] L.J. McGuffin, K. Bryson, D.T. Jones, The PSIPRED protein structure prediction server, *Bioinformatics* 16 (2000) 404–405.
- [38] K. Ichiiyanagi, Y. Ishino, M. Ariyoshi, K. Komori, K. Morikawa, Crystal structure of an archaeal intein-encoded homing endonuclease PI-PfuI, *J. Mol. Biol.* 300 (2000) 889–901.
- [39] L.W. Guddat, J.C. Bardwell, R. Glockshuber, M. Huber-Wunderlich, T. Zander, J.L. Martin, Structural analysis of three His32 mutants of DsbA: support for an electrostatic role of His32 in DsbA stability, *Protein Sci.* 6 (1997) 1893–1900.
- [40] J. Lubkowski, G. Bujacz, L. Boque, P.J. Dommelle, T.M. Handel, A. Wlodawer, The structure of MCP-1 in two crystal forms provides a rare example of variable quaternary interactions, *Nat. Struct. Biol.* 4 (1997) 64–69.
- [41] E.R. Johnson, D.B. McKay, Crystallographic structure of the amino terminal domain of yeast initiation factor 4A, a representative DEAD-box RNA helicase, *RNA* 5 (1999) 1526–1534.
- [42] V. Durbecq, G. Sainz, Y. Oudjama, B. Clantin, C. Bompard-Gilles, C. Tricot, J. Caillet, V. Stalon, L. Droogmans, V. Villeret, Crystal structure of isopentenyl diphosphate:dimethylallyl diphosphate isomerase, *EMBO J.* 20 (2001) 1530–1537.
- [43] T.M. Larsen, M.M. Benning, I. Rayment, G.H. Reed, Structure of the bis( $\text{Mg}^{2+}$ )-ATP-oxalate complex of the rabbit muscle pyruvate kinase at 2.1 Å resolution: ATP binding over a barrel, *Biochemistry* 37 (1998) 6247–6255.
- [44] S. Henikoff, J.G. Henikoff, Performance evaluation of amino acid substitution matrices, *Proteins* 17 (1993) 49–61.
- [45] J.T. Penniston, A. Enyedi, Modulation of the plasma membrane  $\text{Ca}^{2+}$  pump, *J. Membr. Biol.* 165 (1998) 101–109.
- [46] J.D. Thompson, D.G. Higgins, T.J. Gibson, CLUSTAL W: improving the sensitivity of progressive multiple sequence alignment through sequence weighting, position-specific gap penalties and weight matrix choice, *Nucleic Acids Res.* 22 (1994) 4673–4680.
- [47] M.A. Marti-Renom, A.C. Stuart, A. Fiser, R. Sanchez, F. Melo, A. Sali, Comparative protein structure modeling of genes and genomes, *Annu. Rev. Biophys. Biomol. Struct.* 29 (2000) 291–325.
- [48] A.J. MacKerell, B. Brooks, C.L. Brooks III, L. Nilsson, B. Roux, Y. Won, M. Karplus, The Energy Function and its Parameterization with an Overview of the Program, vol. 1, John Wiley and Sons, Chichester, 1998, pp. 271–277.
- [49] I.A. Vakser, O.G. Matar, C.F. Lam, A systematic study of low-resolution recognition in protein–protein complexes, *Proc. Natl. Acad. Sci. U.S.A.* 96 (1999) 8477–8482.
- [50] A. Enyedi, T. Vorherr, P. James, D.J. McCormick, A.G. Filoteo, E. Carafoli, J.T. Penniston, The calmodulin binding domain of the plasma membrane  $\text{Ca}^{2+}$  pump interacts both with calmodulin and with another part of the pump, *J. Biol. Chem.* 264 (1989) 12313–12321.
- [51] C. Schafmeister, W.S. Ross, V. Romanowski, *LeaP*, 1995.
- [52] D. Case, T.A. Darden, T.E. Cheetham, III, C.L. Simmerling, J. Wang, R.E. Duke, R. Luo, K.M. Merz, B. Wang, D.A. Pearlman, M. Crowley, S. Brozell, V. Tsui, H. Gohlke, J. Mongan, V. Hornak, G. Cui, P. Berora, C. Schafmeister, J.W. Caldwell, W.S. Ross, P.A. Kollman, *AMBER 8*, University of California, San Francisco, 2004.
- [53] J. Wang, P. Cieplak, P.A. Kollman, How well does a restrained electrostatic potential (RESP) model perform in calculating conformational energies of organic and biological molecules? *J. Comput. Chem.* 21 (2000) 1049–1074.
- [54] G. Hawkins, C.J. Cramer, D.G. Truhlar, Parameterized models of aqueous free energies of solvation based on pairwise descreening of solute atomic charges from a dielectric medium, *J. Biophys. Chem.* 100 (1996) 1982–19839.
- [55] T. Ferrin, C.C. Huang, L.E. Jarvis, R. Langridge, The Midas display system, *J. Mol. Graph.* 6 (1988) 13–27.
- [56] R. Laskowski, M.W. MacArthur, D.S. Moss, J.M. Thornton, PROCHECK: a program to check the stereochemical quality of protein structures, *J. Appl. Cryst.* 26 (1993) 283–291.
- [57] J. Pontius, J. Richelle, S.J. Wodak, Deviations from standard atomic volumes as a quality measure for protein crystal structures, *J. Mol. Biol.* 264 (1996) 121–136.
- [58] R.W. Hooft, G. Vriend, C. Sander, E.E. Abola, Errors in protein structures, *Nature* 381 (1996) 272.
- [59] K.D. Osborn, A. Zaidi, A. Mandal, R.J. Urbauer, C.K. Johnson, Single-molecule dynamics of the calcium-dependent activation of plasma-membrane  $\text{Ca}^{2+}$ -ATPase by calmodulin, *Biophys. J.* 87 (2004) 1892–1899.